UNCONVENTIONAL RESOURCES TECHNOLOGY CONFERENCE
FUELED BY SPE • AAPG • SEG

URTeC: 5032

Effect of Pore Geometry and Heterogeneous Surface Wettability on the Nanoconfined Phase Behavior in Nanopore Networks of Shale Rocks

Sidian Chen*[1], Jiamin Jiang[2], Bo Guo[1], 1 University of Arizona, 2 Chevron Energy Technology Co.

This paper was prepared for presentation at the Unconventional Resources Technology Conference held in Houston, Texas, USA, 26-28 July 2021.

Abstract

The phase behavior of hydrocarbons in liquid-rich shale formations deviates from their bulk phase behavior due to the nanoconfinement effects in the extensive nanopores of shale rocks. While the phase behavior in nanopores has been widely investigated, the macroscopic phase behavior in the complex nanopore networks of shale rocks remains poorly understood. To address this critical problem, we have recently developed a novel pore-network-based upscaling framework that allows for deriving the macroscopic phase behavior for shale rocks accounting for size- and geometry-dependent nanoconfinement effects (Chen et al., 2021). Here, we apply the pore-network-based upscaling framework to examine the influences of pore geometry and heterogeneous surface wettability on the macroscopic phase behavior using three example nanopore networks. The results show that pore geometry and heterogeneous surface wettability have a relatively minor impact on the macroscopic phase behavior, and (as reported in our prior study) pore size distribution is the primary controlling factor. Conversely, pore geometry and heterogeneous surface wettability are shown to significantly modify the spatial distribution of fluid phases and components in the nanopore networks, which further modifies the two-phase constitutive relationships (e.g., capillary pressure saturation curve and relative permeability saturation curve).

Introduction

Phase behavior plays an important role in hydrocarbon recovery from reservoirs, especially liquid-rich shale reservoirs. In liquid-rich shale reservoirs, the rocks oftentimes contain extensive nanometer-scale pore spaces, within which the phase behavior deviates from the bulk behavior. Such deviation appears to result from the so-called nanoconfinement effects—including large pressure difference across the fluid-fluid interfaces (i.e., capillary pressure) and strong interaction between hydrocarbon molecules and the pore wall (i.e., fluid-wall interaction) as demonstrated by nanofluidic experiments and molecular-level simulations (Luo et al., 2015, Barsotti et al., 2016, Jin and Firoozabadi, 2016, Zhong et al., 2018, Liu and

Zhang, 2019). To date, such experimental insights and molecular-level understandings are challenging to be directly incorporated into reservoir-scale simulations. In the reservoir-scale simulators, the phase behavior is simulated using the so-called phase equilibrium model. The model assumes thermodynamic equilibrium between different fluid phases—i.e., the chemical potential or fugacity is equal among all phases for any prescribed temperature and pressure—such that mathematical formulations can be derived and solved to quantify the phase behavior (Michelsen, 1982a, 1982b). While the standard phase equilibrium model—assuming equal pressure among different fluid phases and no fluid-wall interaction—can successfully simulate the bulk phase behavior, it failed to predict the phase behavior in nanopores.

Several studies have extended the standard phase equilibrium model to account for the nanoconfinement effects including the capillary pressure and fluid-wall interaction. The effect of capillary pressure is included by assigning different pressures to different fluid phases (instead of assigning the same pressure like that in the standard phase equilibrium model) and using the phase pressure to compute the chemical potential or fugacity (Brusilovsky, 1992, Shapiro and Stenby, 2001, Nojabaei et al., 2013, Sandoval et al., 2016). In addition, the fluid-wall interaction can be included by assuming that the interaction introduces additional fluid phases (i.e., adsorbed phases) on the pore wall, which will modify the original fluid compositions and thus the phase behavior (Travalloni et al., 2010, 2014, Sandoval et al., 2018). These extended models have enabled modeling the nanoconfined phase behavior in nanopores. Yet, the phase behavior in the complex nanopore networks within shale rocks is still poorly understood.

To bridge this gap, we recently developed a novel pore-network-based upscaling framework to examine the macroscopic phase behavior in nanopore networks (Chen et al., 2021). Specially, we generalized an extended phase behavior model in a single cylindrical nanopore developed by Sandoval et al., 2018 to pores with different pore geometries (e.g., square tube and triangular tube) and applied the generalized model to each pore of a pore network. Then assuming thermodynamic equilibrium across the nanopore network, upscaled phase behavior formulations were obtained. This pore-network-based upscaling framework has been employed to derive the macroscopic phase behavior in complex nanopore networks. The pores were assumed to be square tubes with uniform surface wettability (i.e., zero contact angle). In natural shale rocks, the pore geometry can be much more complex and surface wettability can be heterogeneous. Such complex pore geometry and heterogeneous surface wettability may lead to further deviation of phase behavior, which remains to be examined.

In the present study, we investigate the impact of pore geometry and heterogeneous surface wettability using the pore-network-based upscaling framework developed by Chen et al., 2021. We first construct three pore networks that consist of different proportions of square-tube and triangular pores and heterogeneous surface wettability (i.e., nonuniform contact angles). Then the upscaling model is applied to those pore networks to derive their macroscopic phase behaviors. To our knowledge, this is the first study about the impact of the pore geometry and heterogeneous surface wettability on the macroscopic phase behavior.

Methods

To provide a basic understanding of the pore-network-based upscaling framework, we conceptually summarize the key derivations and equations here. Additional details can be referred to our prior work (Chen et al., 2021).

In the upscaling framework, we first represent the realistic pore structures in shale rocks using a nanopore network consisting of N_p pores (see **Error! Reference source not found.**). To better represent the realistic pore spaces and pore surface wettability, different pore geometries (e.g., square or triangular tubes) and contact angles are assigned to different pores of the network. When hydrocarbons (N_c components in total) reside in the pore network, they may exist as different fluid phases, i.e., liquid, gas,

and adsorbed phases (see **Error! Reference source not found.**). Within each pore, all three phases (if coexist) are assumed in thermodynamic equilibrium, namely, the

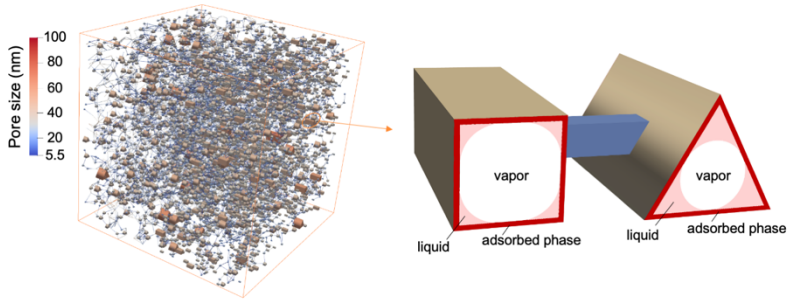

Figure 1. Three-dimensional (3D) representation of a nanopore network and the configuration liquid, gas, and adsorbed phases in a nanopore with a square cross-section and a nanopore with a triangular cross-section.

chemical potential or fugacity of each hydrocarbon component is equal among all phases. Then we assume thermodynamic equilibrium across the pore network, i.e., the chemical potential or fugacity of each hydrocarbon component in each phase, the pressure of each phase, and component composition in each phase are equal among all the pores. Using F to denote the equal fugacity, P to denote the equal phase pressure, and X, Y, W to respectively denote the equal component composition in the liquid, vapor, and adsorbed phases, we can derive the following upscaled phase behavior model for the entire pore network,

$$F^{k,l}(T,P^v,X^k) = F^{k,v}(T,P^l,Y^k) = F^{k,ad}(T,P^{ad},W^k). \tag{1}$$

where the functional forms of $F^{k,l}$ and $F^{k,v}$ are given based on the Peng-Robinson equation of state and the functional forms of $F^{k,ad}$ is given by a simple multicomponent Langmuir model,

$$\begin{cases} W^k = \Xi^k/(\Sigma_{k=1}^{N_c}\Xi^k), \\ \Xi^k = \Sigma_{i=1}^{N_p}\xi_i^k = \sum_{i=1}^{N_p}\xi_i^{k,max}(T)\dfrac{b_i^k(T)F^{k,ad}}{1+\Sigma_{j=1}^{N_c}b_i^j(T)F^{j,ad}}, \end{cases} \tag{2}$$

where Ξ^k is the total amount of component k in the adsorbed phase, ξ_i^k is the amount of component k in the adsorbed phase in pore i, $\xi_i^{k,max}$ is the maximum amount of component k in the adsorbed phase in pore i, b_i^k is the adsorption equilibrium constant of component k in pore i.

In addition, when liquid and vapor phases coexist, they will form curved interfaces leading to pressure differentials between the two phases (i.e., capillary pressure). The relationship between liquid pressure, vapor pressure, and capillary pressure is given by Equation (3), where capillary pressure is assumed to follow the Young-Laplace equation.

$$P^v - P^l = P^c(S^l) = \frac{\sigma}{R_m(S^l)}, \tag{3}$$

where σ is the interfacial tension, R_m is the radius of liquid-vapor interface meniscus curvature which is a function of the liquid phase saturation S^l in the pore network.

The $R_m - S^l$ relationship depends on the pore network structures, including the pore size distribution, pore geometry, and contact angle. In the prior work, we have derived the functional form of R_m for pore networks with square-tube pore and zero contact angle (Chen et al., 2021). Here we generalize the expression of R_m to account for nonuniform pore geometries and contact angles following the similar procedure. The only difference is that instead of numbering the pores according to their sizes like that in Chen et al., 2021, here we need to number the pores from 1 to N_p in terms of the radius of liquid-vapor interface meniscus curvature when the interfaces meet in the pore (denoted by r'_m) such that $r'_{m,j} \leq$

$r'_{m,j+1}$ where $j = 1, \dots, N_p$. If multiple pores have the same r'_m, they are numbered next to each other. Then following the same procedure, we arrive at a similar expression of R_m as shown in the following,

$$R_m(S^l) = \begin{cases} \left(\dfrac{S^l(V - V^{ad}) - \Sigma_{j=1}^{i-1}(v_j - v_j^{ad})}{\Sigma_{j=i}^{N_p} l_j \tilde{a}_{m,j}} \right)^{1/2} & S^l_{s,i-1} < S^l \le S^l_{c,i}, \\ r'_{m,i} & S^l_{c,i} < S^l \le S^l_{s,i}. \end{cases} \quad (4)$$

where V is the total pore volume, V^{ad} is the total adsorbed phase volume; v_j is the volume of pore j, v_j^{ad} is the adsorbed phase volume in pore j, l_j is the length of pore j, $\tilde{a}_{m,j}$ is the liquid phase area in the cross-sectional plane of pore j when the radius of liquid-vapor interface meniscus curvature is equal to 1, the subscript i refers to the pore has the smallest r'_m among pores that has both liquid and gas phases, $S^l_{c,i}$ is the liquid phase saturation in the pore network before the liquid-vapor interfaces meet in pore i, $S^l_{s,i}$ is the liquid phase saturation in the pore network when the liquid-vapor interfaces meet in pore i. Note that the expressions of $S^l_{c,i}$ and $S^l_{s,i}$ are similar to that of Chen et al., 2021, except that here pore i is the pore that has the smallest r'_m (if multiple pores have the same r'_m, then i is equal to the smallest number) among pores that has both liquid and gas phases, instead of the pore that has the smallest size among those pores like that in the work of Chen et al., 2021.

Equations (1-4) summarize the key mathematical formulations for the upscaling model. They can be solved by a modified flash calculation which is similar to the standard flash calculation. The only difference is that in the modified flash calculation, one of the bulk phases (e.g., liquid pressure if vapor pressure is prescribed) and the composition in the bulk phases are unknown and need to be solved. More details can refer to Chen et al., 2021.

Results and discussion

We first generate three nanopore networks with heterogeneous pore geometries and surface wettability and then apply the upscaling framework to these nanopore networks to examine the impacts of pore geometry and surface wettability on the macroscopic phase behavior. Phase envelopes of two example mixture systems (i.e., a binary mixture system and a ternary mixture system) and the spatial distributions of fluid phases and components are compared and discussed.

Pore network construction

An unstructured nanopore network consisting of 1000,000 pores is generated to represent the realistic pore structure in shale rocks using the method presented by the work of Qin et al., 2019 and Qin and van Brummelen, 2019. The nanopore network consists of pores interconnected by throats. The pore size follows a log-normal distribution with an average size of 10 nm (see **Error! Reference source not found.**a). To examine the effects of pore geometry and surface wettability on the macroscopic phase behavior, a reference pore network (denoted by PN #0) is first constructed such that all pores are square tubes with zero contact angles. Then

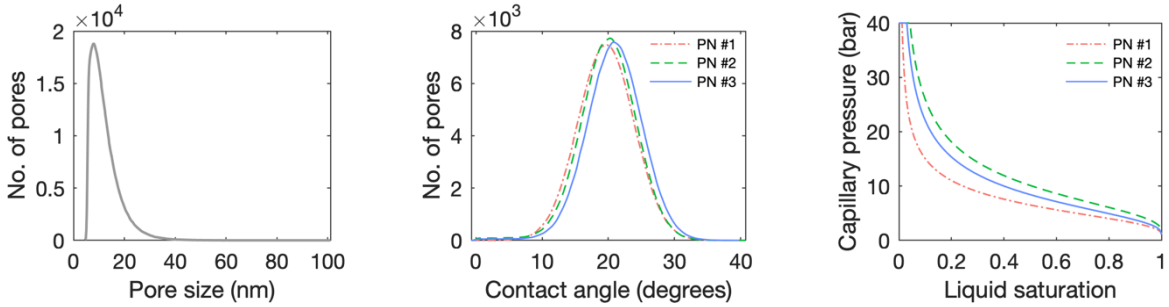

Figure 2. (a) Pore size distribution, (b) contact angle distribution, and (c) capillary pressure saturation curves for three example pore networks, namely, PN #1, PN #2, and PN #3. Note that while the pore size distribution is kept the same for all three pore networks, the pore geometries and contact angles are different. Each pore network has a different fraction of square- and triangular-tube pores (i.e., PN #1 consists of 100% square-tube pores, PN #2 consists of 100% triangular-tube pores, PN #3 consists of 50% square-tube pores and 50% triangular-tube pores) with randomly assigned contact angles whose distributions are shown in (b).

three additional pore networks with different pore geometries and contact angles are constructed. The pore geometries are designed as the following: (1) all pores are set to be square tubes (denoted by PN #1); (2) half of pores are set to be square tubes, while the others are set to triangular tubes (denoted by PN #2), (3) all pores are set to be triangular tubes (denoted by PN #3). Then in the three additional pore networks, nonuniform contact angles—which are assumed to follow a Gaussian distribution (Alhammadi et al., 2017) as shown in **Error! Reference source not found.**b—are randomly assigned to all pores in each pore network. Because the different pore geometries and contact angles will lead to different capillary pressure saturation curves, we also present the capillary pressure saturation curves for the three pore networks in **Error! Reference source not found.**c using an interfacial tension of 0.02 N/m as an example.

Effects of pore geometry and surface wettability on the macroscopic phase envelope

We then apply the pore-network-based upscaling framework to compute the macroscopic phase envelopes for three nanopore networks with different pore geometries and nonuniform contact angles (i.e., PN #1, PN#2, and PN#3) using the phase envelope of a nanopore network with only square-tube pores and zero contact angle (i.e., PN #0) for reference. Two example hydrocarbon mixtures are simulated including a binary mixture (C1:C4 = 0.5:0.5) and a ternary mixture (C1:C4:C10 = 0.42:0.33:0.25). The thermodynamic properties of C1, C4, and C10 (e.g., the critical pressure, the critical volume, the critical temperature, the acentric factor, and the molar weight) are obtained from Pedersen et al., 2006 and Sandoval et al., 2018.

The macroscopic phase envelopes are presented for the reference nanopore network and the three nanopore networks in **Error! Reference source not found.**. For a given system (either binary mixture system or ternary mixture system), the phase envelopes are almost overlapped for all four nanopore networks. This indicates that the pore geometry and contact angle have a minimal impact on the macroscopic phase envelope. The reason is the following. As revealed by Chen et al., 2021, the effect of capillary pressure on the macroscopic phase envelope is much less important than that of adsorption (which increases with specific surface area, i.e., pore surface area per volume). While pore geometry and contact angle may significantly change the capillary pressure saturation curve, they may not significantly change the specific surface area for adsorption. Therefore, as long as the specific surface area—which mainly depends on the pore size distribution—is kept the same or close among different networks, the impact of adsorption and thus the macroscopic phase envelope will be similar among those networks.

(a) Binary mixture system

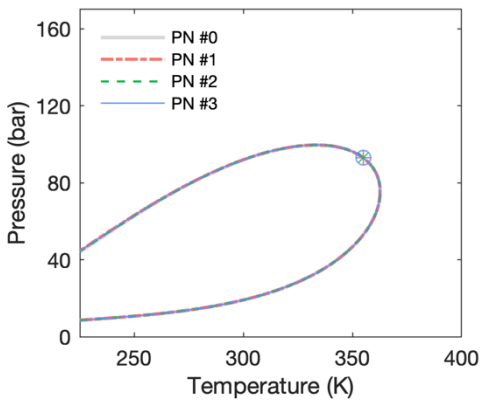

(b) Ternary mixture system

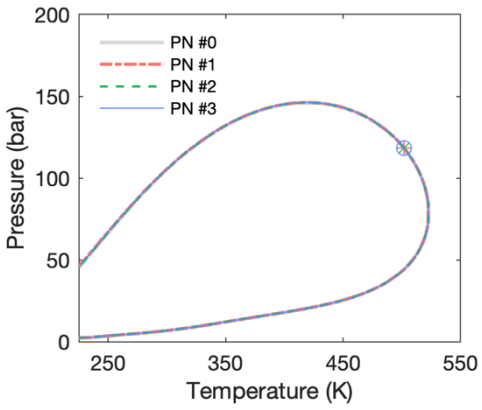

Figure 3. Phase envelopes of (a) a binary mixture system (i.e., C1 and C4 with a molar ratio of 0.5:0.5) and (b) a ternary mixture system (i.e., C1, C4, and C10 with a molar ratio of 0.42:0.33:0.25) in three pore networks that have different proportions of square-tube and triangular-tube pores with nonzero nonuniform contact angles (i.e., PN #1, PN #2, and PN #3). The phase envelops in a pore network whose pores are square tubes with zero contact angles (i.e., PN #0) are presented as a reference.

Effects of pore geometry and surface wettability on the spatial distributions of fluid phases and components

We conduct a closer inspection of the effect of pore geometry and surface wettability on the phase behavior by examining the spatial distributions of fluid phases and components in the three nanopore networks with different pore geometries and contact angles (i.e., PN #1, PN#2, and PN#3). For the binary mixture system, the spatial distributions of fluid phases and components at an example temperature (330 K) and pressure (70 bar) are presented for all three nanopore networks (see Figures 4 and 5). The result shows that the spatial distribution of fluid and component is controlled by not only the pore size distribution as revealed by Chen et al., 2021, but also the pore geometry and contact angle. Similar to Chen et al., 2021, the liquid saturation, the molar ratio of heavy to light component (i.e., the molar ratio of C4 to C1) in the bulk phases (i.e., liquid and gas phases), and the molar ratio of heavy to light component in all three phases are in general greater in the pores whose sizes are smaller (see Figure 4). But the dependence of fluid and component distribution on pore size varies in different pore networks due to their different pore geometries and contact angles.

To better interpret the results, we present for each network the spatial distributions of fluid phases and components in pores with the same contact angle (three example contact angles, i.e., θ=15°, θ=20°, and θ=25°, are used) in Figure 5. The results show that when only square-tube pores exist (e.g., PN #1), the liquid saturation and ratio of C4 to C1 are always greater in the equal-contact-angle pores with smaller sizes, while they are always greater in the equal-size pores with smaller contact angles. For instance,

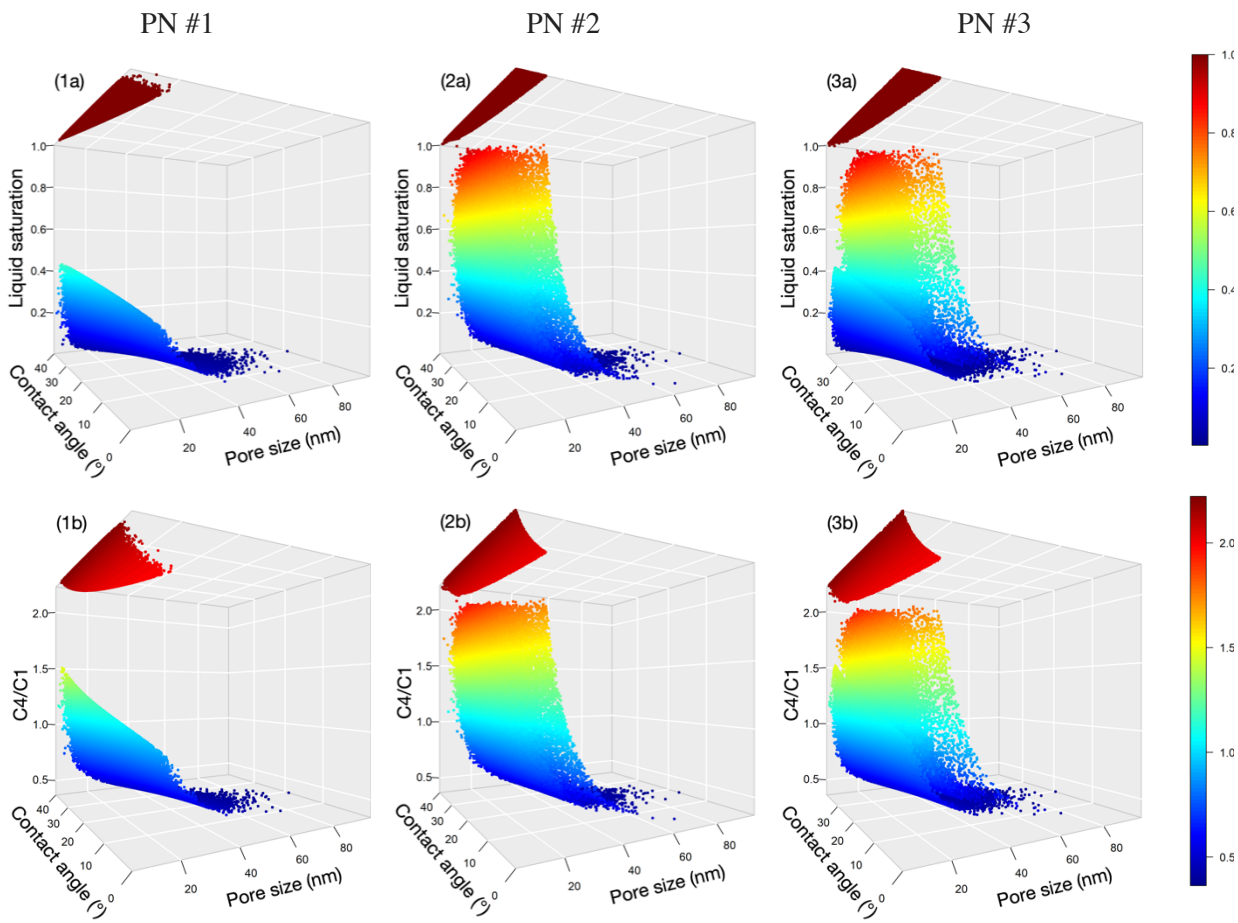

Figure 4. Spatial distributions of (a) liquid phase saturation and (b) molar ratio of C4 to C1 in (1) PN #1, (2) PN #2, and (3) PN #3. The distributions are demonstrated at an example temperature (330 K) and pressure (70 bar).

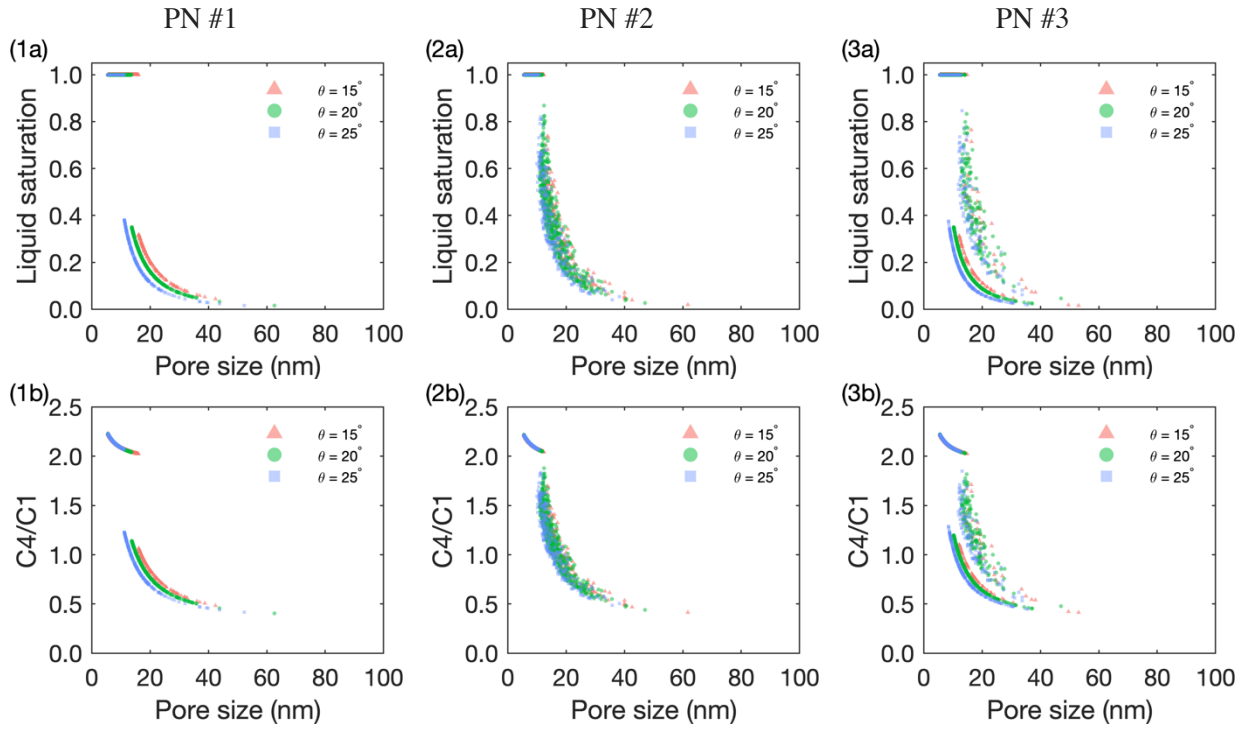

Figure 5. Spatial distributions of (a) liquid phase saturation and (b) molar ratio of C4 to C1 in pores with the same contact angle ($\theta = 15°$, $\theta = 20°$, and $\theta = 25°$ are selected as examples). Each column represents the results in a different pore network, i.e., (1) PN #1, (2) PN #2, and (3) PN #3. The distributions are demonstrated at an example temperature (330 K) and pressure (70 bar).

among the pores with θ=15°, the liquid saturation and the ratio of C4 to C1 in the smallest pore are 22.6 times and 4.6 times greater than those in the largest pore, respectively; while among the pores with a pore size of 20 nm, the liquid saturation and the ratio of C4 to C1 in the pore with θ=15° are 1.3 times and 1.8 times greater than those in the largest pore with θ=25°, respectively. This is because more liquid—that has a greater molar ratio of C4 to C1 than the vapor—will reside in the pores with smaller sizes and contact angles due to their greater capillary pressure and stronger liquid wettability. In addition, the preferential adsorption of C4 in the smaller pores will further increase the ratio. On the other hand, when triangular-tube pores exist (e.g., PN #2 and PN #3), though the liquid saturation and the ratio of C4 to C1 appear in general greater in pores with smaller sizes or contact angles, they do not show monotonic relationships as observed in PN#1. This is because the irregular triangular shapes of those pores will modify their capability to hold liquid phase at the corners (e.g., a corner with a smaller angle can hold a greater liquid volume than that with a larger angle for the same capillary pressure) and their specific surface area for adsorption. Take PN #3 for example, the liquid saturation and the ratio of C4 to C1 in the triangular-tube pores are 1.5 times and 2.6 times greater than those in the square-tube pores, respectively. Such differences in spatial distributions of fluid and components will lead to different constitutive relationships (e.g., capillary pressure saturation curves and relative permeability saturation curves), which will eventually affect two-phase displacement processes.

For the ternary mixture system, the spatial distributions of fluid phases and components at an example temperature (450 K) and pressure (70 bar) are presented for all three pore networks in Figure 6. Similar to the binary mixture system, when only square-tube pores exist, the liquid saturation and ratio of C4 to C1 are always greater in the equal-contact-angle pores with smaller sizes, while they are always greater in the equal-size pores with smaller contact angles (e.g., PN#1). when triangular-tube pores exist (e.g., PN #2 and PN #3), the liquid saturation and the ratio of C4 to C1 also have nonmonotonic relationships as observed in PN#1. This confirms the dependence of spatial distributions of fluid phases and components—and thus constitutive relationships—on the complex pore-scale heterogeneity (e.g., pore size distribution, pore geometry, and contact angle).

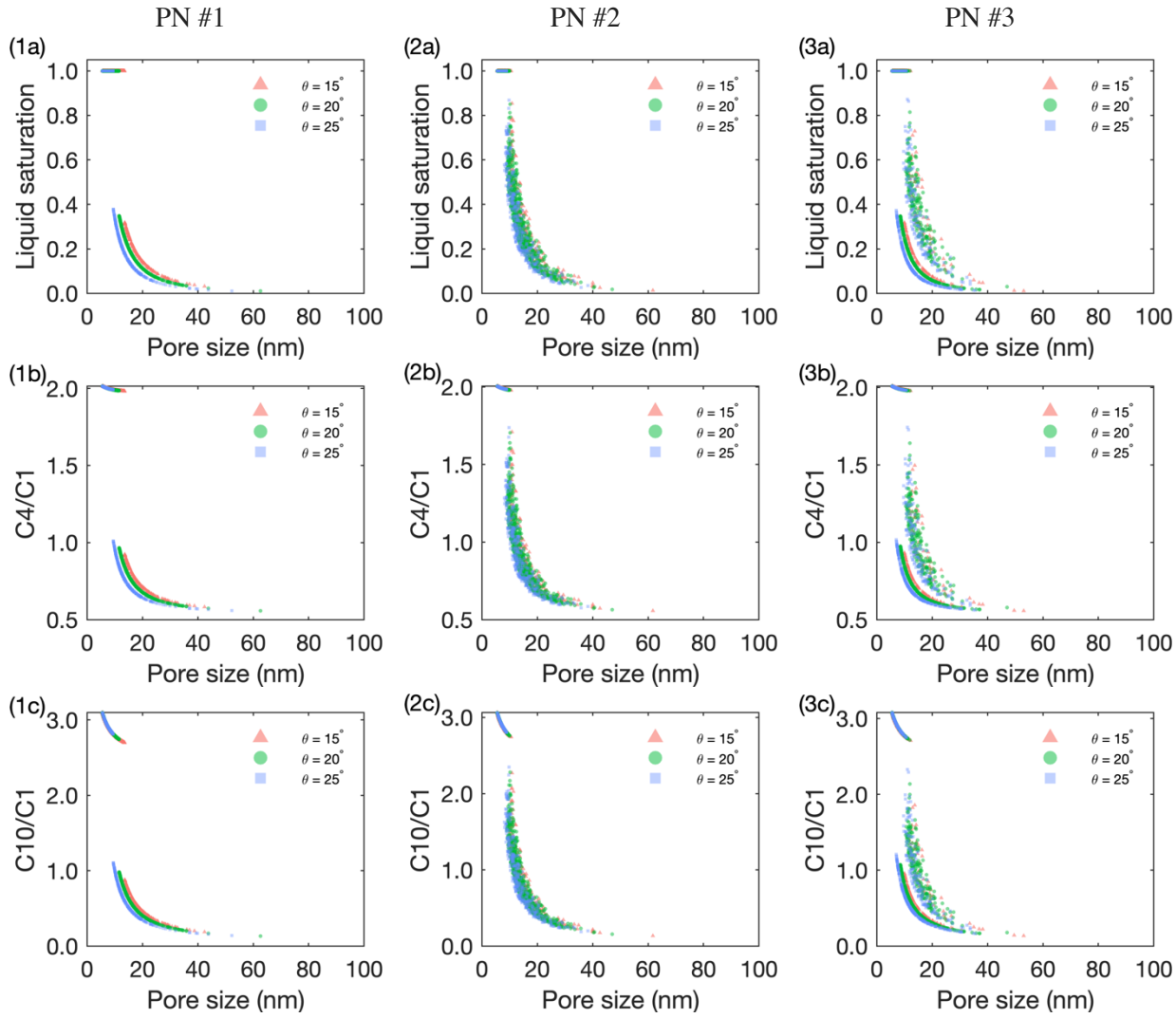

Figure 6. Spatial distributions of (a) liquid phase saturation, (b) molar ratio of C4 to C1, and (c) molar ratio of C10 to C1 in pores with the same contact angle ($\theta = 15°$, $\theta = 20°$, and $\theta = 25°$ are selected as examples). Each column represents the results in a different pore network, i.e., (1) PN #1, (2) PN #2, and (3) PN #3. The distributions are demonstrated at an example temperature (450 K) and pressure (70 bar).

Conclusions

We have applied a novel pore-network-based upscaling framework to study the effects of pore geometry and heterogeneous surface wettability on the macroscopic phase behavior in shale rocks. The phase behavior in three example nanopore networks with different pore geometries and nonuniform contact angles were simulated and compared. The main findings are summarized in the following.

(1) The macroscopic phase envelopes in the three nanopore networks with different pore geometries and heterogeneous surface wettability (i.e., nonuniform contact angles) overlap with that in the network with uniform pore geometry and surface wettability (i.e., zero contact angles). Thus the pore geometry and heterogeneous surface wettability have a minor impact on the macroscopic phase behavior, which confirms that the pore size distribution—as reported by Chen et al., 2021—is the primary factor that controls macroscopic phase behavior.

(2) Pore geometry and surface wettability significantly modify the spatial distribution of fluid phases and components in a pore network. In our simulations, triangular-tube pores have a greater liquid saturation (approximately 1.5 times) and a greater ratio of heavier to lighter components (approximately 2.6 times)

than square-tube pores, and pores with smaller contact angles (e.g., θ=15°) have a greater liquid saturation (approximately 1.3 times) and a greater ratio of heavier to lighter components (approximately 1.8 times) than pores with greater contact angles (e.g., θ=25°). Such differences in distributions of phases and components can lead to significantly different constitutive relationships (e.g., capillary pressure saturation curves and relative permeability saturation curves) and thus affect two-phase displacement processes.

Acknowledgment

This work was supported by the Water, Environmental, and Energy Solutions (WEES) Initiative at the University of Arizona. We thank Dr. Chaozhong Qin for providing the pore-network generation code.

References

Alhammadi, A. M., AlRatrout, A., Singh, K., Bijeljic, B. and Blunt, M. J., 2017. In situ characterization of mixed-wettability in a reservoir rock at subsurface conditions. *Scientific Reports*, *7*(1), 1-9.

Barsotti, E., Tan, S. P., Saraji, S., Piri, M. and Chen, J. H., 2016. A review on capillary condensation in nanoporous media: Implications for hydrocarbon recovery from tight reservoirs. *Fuel*, *184*, 344-361.

Brusilovsky, A.I., 1992. Mathematical simulation of phase behavior of natural multicomponent systems at high pressures with an equation of state. *SPE reservoir engineering*, *7*(01), 117-122.

Chen, S., Jiang, J. and Guo, B., 2021. A pore-network-based upscaling framework for the nanoconfined phase behavior in shale rocks. *Chemical Engineering Journal*, *417*, 129210.

Liu, X. and Zhang, D., 2019. A review of phase behavior simulation of hydrocarbons in confined space: Implications for shale oil and shale gas. *Journal of Natural Gas Science and Engineering*, *68*, 102901.

Jin, Z. and Firoozabadi, A., 2016. Thermodynamic modeling of phase behavior in shale media. *Spe Journal*, *21*(01), 190-207.

Luo, S., Lutkenhaus, J. L. and Nasrabadi, H., 2015, September. Experimental study of confinement effect on hydrocarbon phase behavior in nano-scale porous media using differential scanning calorimetry. In *SPE annual technical conference and exhibition*. Society of Petroleum Engineers.

Michelsen, M. L., 1982a. The isothermal flash problem. Part I. Stability. *Fluid phase equilibria*, *9*(1), 1-19.

Michelsen, M. L., 1982b. The isothermal flash problem. Part II. Phase-split calculation. *Fluid phase equilibria*, *9*(1), 21-40.

Nojabaei, B., Johns, R. T. and Chu, L., 2013. Effect of capillary pressure on phase behavior in tight rocks and shales. *SPE Reservoir Evaluation & Engineering*, *16*(03), 281-289.

Qin, C. Z., Guo, B., Celia, M. and Wu, R., 2019. Dynamic pore-network modeling of air-water flow through thin porous layers. *Chemical Engineering Science*, *202*, 194-207.

Qin, C. Z. and van Brummelen, H., 2019. A dynamic pore-network model for spontaneous imbibition in porous media. *Advances in Water Resources*, *133*, 103420.

Sandoval, D. R., Yan, W., Michelsen, M. L. and Stenby, E. H., 2016. The phase envelope of multicomponent mixtures in the presence of a capillary pressure difference. *Industrial & Engineering Chemistry Research*, *55*(22), pp.6530-6538.

Sandoval, D. R., Yan, W., Michelsen, M. L. and Stenby, E. H., 2018. Influence of adsorption and capillary pressure on phase equilibria inside shale reservoirs. *Energy & fuels*, *32*(3), pp.2819-2833.

Shapiro, A. A. and Stenby, E. H., 2001. Thermodynamics of the multicomponent vapor–liquid equilibrium under capillary pressure difference. *Fluid Phase Equilibria*, *178*(1-2), 17-32.

Travalloni, L., Castier, M., Tavares, F. W. and Sandler, S. I., 2010. Thermodynamic modeling of confined fluids using an extension of the generalized van der Waals theory. *Chemical Engineering Science*, *65*(10), 3088-3099.

Travalloni, L., Castier, M. and Tavares, F. W., 2014. Phase equilibrium of fluids confined in porous media from an extended Peng–Robinson equation of state. *Fluid Phase Equilibria*, *362*, 335-341.

Zhong, J., Riordon, J., Zandavi, S. H., Xu, Y., Persad, A. H., Mostowfi, F. and Sinton, D., 2018. Capillary condensation in 8 nm deep channels. *The journal of physical chemistry letters*, *9*(3), 497-503.